

Infrared Spectroscopy and Optical Constants of Porous Amorphous Solid Water[†]François Cholette,[‡] Tykhon Zubkov,^{§,⊥} R. Scott Smith,[§] Zdenek Dohnálek,[§] Bruce D. Kay,^{*,§} and Patrick Ayotte^{*,‡}*Fundamental and Computational Sciences Directorate, Pacific Northwest National Laboratory, P.O. Box 999, Mail Stop K8-88, Richland, Washington 99352, and Département de chimie, Université de Sherbrooke, 2500 Boulevard Université, Sherbrooke, Québec, Canada J1K 2R1**Received: July 29, 2008; Revised Manuscript Received: September 17, 2008*

Reflection–absorption infrared spectra (RAIRS) of amorphous solid water (ASW) films grown at 20 K on a Pt(111) substrate at various angles ($\theta_{\text{Beam}} = 0\text{--}85^\circ$) using a molecular beam are reported. They display complex features arising from the interplay between refraction, absorption within the sample, and interference effects between the multiple reflections at the film–substrate and film–vacuum interfaces. Using a simple classical optics model based on Fresnel equations, we obtain optical constants [i.e., $n(\omega)$ and $k(\omega)$] for porous ASW in the 1000–4000 cm^{-1} (10–2.5 μm) range. The behavior of the optical properties of ASW in the intramolecular OH stretching region with increasing θ_{Beam} is shown to be strongly correlated with its decreasing density and increasing surface area. A direct comparison between the RAIRS and calculated vibrational spectra shows a large difference ($\sim 200\text{ cm}^{-1}$) in the position of the coupled H-bonded intramolecular OH stretching vibrations spectral feature. Moreover, this band shifts in opposite directions with increasing θ_{Beam} in RAIRS and vibrational spectra demonstrating RAIRS spectra cannot be interpreted straightforwardly as vibrational spectra due to severe optical distortions from refraction and interference effects.

I. Introduction

Amorphous solid water (ASW) is an important substrate and matrix for the chemistry of the interstellar medium (ISM).^{1–3} For example, it is believed to be an important constituent of the complex molecular solids, or ices, that form comets, the frosty mantle of interstellar dust grains in cold and dense molecular clouds that shrouds protostellar and protoplanetary regions, as well as at the surface of cold outer solar system objects.^{1–5} Depending on a variety of factors including the local temperature, incident H_2O flux, incidence angle, and kinetic energy, crystalline or amorphous ices formed by vapor condensation can have various amounts of porosity. Therefore, physical data obtained using molecular beam methods^{6–8} are crucial to accurately model the growth and properties of these molecular solids.^{9,10} Interstellar ices may also be contaminated by other condensable material either during their growth or by subsequent adsorption and uptake within their porous structure. Clearly, the interaction of gas phase molecules with dust grains in the ISM will depend greatly on the morphology and microstructure of their ASW mantle.^{11–14} Increasingly detailed models of the structure, morphology, and composition of the icy coating on interstellar grains are continuously being developed based on the interpretation of spectroscopic observations of the ISM. Consequently, accurate optical constants obtained through laboratory studies of condensed water substances as astrophysical ices surrogates^{15–17} are essential for an accurate interpretation of spectroscopic data, for example

those from the Infrared Space Telescope (ISO),¹⁸ or from planetary probes such as those recently provided from the surface of Enceladus by Cassini.¹⁹

Significant challenges exist in the characterization of vapor-deposited condensed water substances in the laboratory which account for most of the disagreement in the literature about their properties. Appropriate methods need to be developed for controlled and reproducible growth and the nondestructive characterization of these fragile nanoporous materials. We have shown that the structure and morphology of ASW films can be best controlled using molecular beam deposition techniques.^{20–27} Specifically, rational synthesis of nanoporous ASW films of specifically controlled crystallinity,²⁵ density,²⁶ porosity,^{21,22} and surface area^{23,24} can be achieved by simply controlling the incidence angle,²⁰ flux, and kinetic energy²⁷ of gas phase H_2O molecules impinging on a cold substrate. Optical interferometry²⁶ and reflection–absorption infrared spectroscopy (RAIRS)^{25,27} as well as adsorption of weakly physisorbed molecules (N_2 , CH_4 , Ar, CO, O_2)^{20–24} have been used to probe the structure and morphology of molecular beam-deposited nanoporous ASW. Further, the complex coupled adsorption, desorption, transport and uptake kinetics of these weakly physisorbed species within nanoporous ASW films have been studied in great detail.^{23,24}

In this work, we used a H_2O molecular beam to prepare (nominally) 100 monolayers (ML) coverage (dense ASW equivalent) films at 20 K on a Pt(111) single crystal substrate as a function of deposition incidence angle. These growth conditions yield highly reproducible morphologies for which quantitative evaluation of the sample's macroscopic density²⁶ and surface area^{23,24} were previously reported using optical interferometry and nitrogen adsorption, respectively. RAIRS characterization was performed on these nanoscopic films and their optical constants were extracted using a simple classical optics model.^{28,29} This procedure is required in order to untangle

[†] Part of the special section “Aqueous Solutions and Their Interfaces”.

* To whom correspondence should be addressed. (P.A.) E-mail: Patrick.Ayotte@USherbrooke.ca. Phone: (819) 821-7889. Fax (819) 821-8017. (B.D.K.) E-mail: Bruce.Kay@pnl.gov. Phone: (509) 371-6143. Fax: (509) 371-6145.

[‡] Université de Sherbrooke.[§] Pacific Northwest National Laboratory.[⊥] Present address: Department of Chemistry, Ball State University, Muncie, IN 47306.

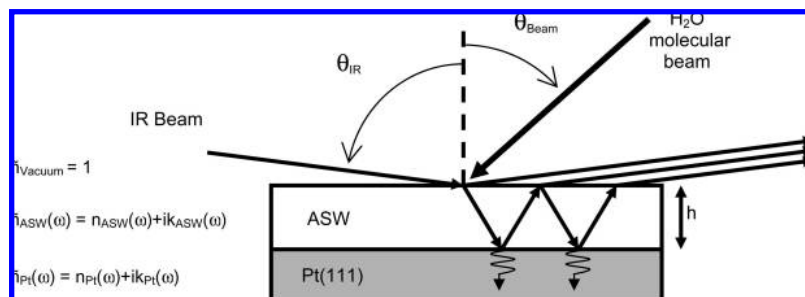


Figure 1. Schematic of the experimental setup used to synthesize and perform spectroscopic characterization of nanoscopic porous ASW films. Films were grown by applying a constant exposure corresponding to a (nominal) coverage of 100 ML (dense ASW equivalent) using an effusive molecular beam [average kinetic energy 5 kJ/mol, flux = $(0.87 \text{ ML/sec}) \cdot \cos \theta_{\text{Beam}}$] at an incident angle θ_{Beam} with respect to the normal of the Pt(111) single crystal substrate at $T = 20 \text{ K}$. These conditions yield a macroscopic density $\rho_{\text{ASW}}(\theta_{\text{Beam}})$ and a thickness of $h = 100 \text{ ML} \cdot [\rho_{\text{ASW}}(\theta_{\text{Beam}} = 0^\circ) / \rho_{\text{ASW}}(\theta_{\text{Beam}})]$. Reflection absorption infrared spectroscopy (RAIRS) is performed by focusing unpolarized light from a FTIR spectrometer at $\theta_{\text{IR}} = 82^\circ$ incidence angle onto the substrate. Experimental absorbance spectra are reported using reflectivities from the film/substrate system [i.e., $I(\omega)$] and from the clean Pt(111) substrate [i.e., $I_0(\omega)$]: $A(\omega) = -\log[I(\omega)/I_0(\omega)]$. Optical constants for nanoporous ASW are obtained using a simple classical optics model (see text) that describes, using Fresnel coefficients, the reflectivity of infrared radiation by infinite parallel interfaces between vacuum, a nanoporous ASW film of absolute thickness h and frequency-dependent complex index of refraction $\tilde{n}_{\text{ASW}}(\omega)$, condensed on an optically thick platinum substrate with frequency-dependent complex index of refraction $\tilde{n}_{\text{Pt}}(\omega)$.

the trivial refraction and interference effects, inherent to RAIRS spectroscopy,^{30–32} from chemically relevant absorption within the nanoscopic films. The amplitude of the spectroscopic signatures from coupled H-bonded and dangling OH intramolecular stretching vibrational modes in the optical parameters of nanoporous ASW are observed to correlate strongly with its density and surface area, respectively.

II. Experimental Section

All experiments were performed in a previously described apparatus,^{21,22} which is a stainless steel ultrahigh vacuum (UHV) chamber with a base pressure of $<1 \times 10^{-10}$ Torr. The chamber is pumped with an 800 L/s turbomolecular pump and is equipped with an ion sputter gun, an Auger electron spectrometer (AES), low energy electron diffraction (LEED) optics, a quadrupole mass spectrometer, and a Fourier transform infrared (FTIR) spectrometer.

The substrate was a Pt(111) disk, 10 mm in diameter and 1 mm thick. It was mounted on 2 mm diameter Ta wires that were clamped in a Au-plated Cu jig attached to the coldfinger of a closed-cycle helium cryostat. The substrate could be cooled to 20 K or resistively heated to above 1300 K. Its temperature was measured with a chromel–alumel thermocouple. Absolute temperature calibration was done using the desorption of N_2 and H_2O multilayers.³³ The substrate was prepared by Ne^+ ion sputtering (1.5 keV, 1.3 μA , 30 min) followed by cycles of oxidative treatment (1×10^{-6} Torr O_2 , 900 K, 300 s) and annealing in UHV (1200 K, 5 s). Surface order and cleanliness of the substrate were checked, respectively, with LEED and AES. Prior to each experiment series, a temperature-programmed desorption (TPD) spectrum of 1 ML of H_2O , defined as the saturation coverage on Pt(111), was recorded and compared against similar spectra from the clean sample.³⁴ This comparison was found to be a good indicator of sample cleanliness.

ASW films were deposited on Pt(111) at 20 K from the saturated vapor pressure of ultrapure deionized water (resistivity $> 18 \text{ M}\Omega/\text{cm}$) using a quasieffusive, room temperature (5 kJ/mol average kinetic energy), molecular beam. The water vapor (2 Torr) was expanded through a 1 mm diameter aperture, and the resulting beam was triply differentially pumped. The H_2O beam flux was $\sim 0.87 \text{ ML/s}$ for normal incidence and scaled with deposition angle, θ_{Beam} , as $\cos \theta_{\text{Beam}}$. The beam was well collimated but broad enough to cover the entire sample at all

θ_{Beam} as schematically shown in Figure 1. Under these conditions, H_2O molecules stick to ice and Pt(111) with essentially unit probability for all θ_{Beam} .^{6,7} A H_2O exposure that produced the characteristic TPD spectrum of a saturated first monolayer coverage of H_2O on Pt(111) was defined as 1 ML H_2O .³⁴ Porous ASW films having a constant coverage of 100 ML were deposited at various θ_{Beam} by adjusting the dose times according to the incidence angle-dependent molecular beam flux yielding a constant exposure of 100 ML dense ASW equivalents (i.e., dose time at θ_{Beam} given by $115\text{s}/\cos \theta_{\text{Beam}}$). This coverage represents a compromise between the long dose times that are required at the most grazing incidences and the improving signal-to-noise ratio resulting from the spectroscopy and analysis of thicker films. As the films' porosity develops from increasing initial surface roughness, very thin films ($h < 10 \text{ ML}$) do not have the fully developed porosity that characterizes films hundreds of ML thick.²⁷ Therefore, the complex sample morphological features and resulting physical properties which results in severe spectral distortions reported here do not apply to films 1–10 ML thick.

RAIRS was performed *in situ* at grazing angle, $\theta_{\text{IR}} = (82 \pm 1)^\circ$, using unpolarized light from a commercial FTIR spectrometer (Bruker Equinox 55). An external optical bench described previously²⁵ included mirrors, KBr windows and lenses for focusing the unpolarized infrared beam onto the sample and collecting the reflected light onto a narrow-band HgCdTe detector (MCT, model 313). Infrared spectra were acquired at 4 cm^{-1} resolution by averaging 2000 scans ($\sim 8 \text{ min}$) at 20 K. Absorbance spectra are reported as $A(\omega) = -\log[I(\omega)/I_0(\omega)]$ using the reflectivity of the film/substrate system $[I(\omega)]$ and that of the clean Pt(111) substrate $[I_0(\omega)]$, both recorded at 20 K across the $\omega = 800\text{--}6500 \text{ cm}^{-1}$ effective spectral range of the spectrometer.

RAIRS spectra of nanoscopic films display complex features arising from refraction, from interference effects (arising from the multiple reflections at the film–vacuum and the film–substrate interfaces), as well as from absorption within the film as shown schematically in Figure 1.^{30–32} Analysis of the RAIRS spectra was performed using a simple classical optics model. Specifically, the model describes the interaction of the incident IR beam at the various interfaces using the polarization- and frequency-dependent Fresnel reflection and transmission coefficients. These are used to calculate the substrate and film/substrate system unpolarized reflectivities, $R(\omega) = 1/2 [R_s(\omega) + R_p(\omega)]$, where

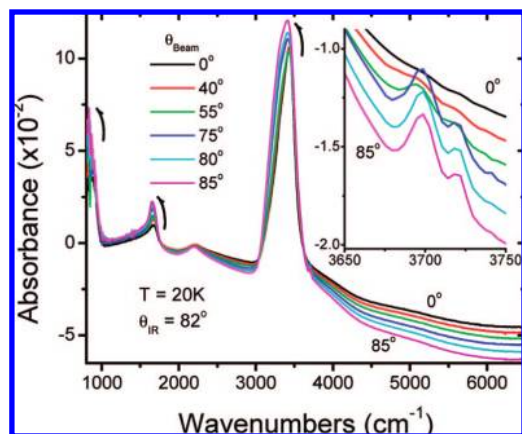


Figure 2. Selected raw absorbance spectra recorded at $T = 20$ K and $\theta_{\text{IR}} = 82^\circ$ for (nominally) 100 ML (dense ASW equivalent) coverage nanoporous ASW films grown on Pt(111) at $T = 20$ K with an effusive H_2O molecular beam at $\theta_{\text{Beam}} = 0, 40, 55, 75, 80$, and 85° . Inset: expanded view of the dangling OH stretching vibrational features assigned to three- (i.e., DAA) and two- (i.e., DA) coordinated water molecules.

R_s and R_p represent the s- and p-polarized reflectivities.^{28,29} Optical constants for platinum from the literature [i.e., the real and imaginary part of its frequency-dependent complex index of refraction, $\tilde{n}_{\text{Pt}}(\omega) = n_{\text{Pt}}(\omega) + ik_{\text{Pt}}(\omega)$]³⁵ are used to calculate the substrate unpolarized reflectivity, $R_{\text{Pt}}(\omega)$. Fresnel spectra (i.e., $A(\omega) = -\log [R_{\text{ASW/Pt}}(\omega)/R_{\text{Pt}}(\omega)]$) are then least-squares fitted to experimental absorbance spectra while iteratively adjusting the ASW films optical constants [i.e., $\tilde{n}_{\text{ASW}}(\omega) = n_{\text{ASW}}(\omega) + ik_{\text{ASW}}(\omega)$] until convergence. The real and imaginary parts of the complex index of refraction of ASW throughout the 800–6500 cm^{-1} range were constrained using the Kramers–Kronig (KK) relation.^{28,29} The effect of the incompleteness of the KK transform (arising from the limited spectral coverage at $\omega < 800$ cm^{-1} due to the transmission cutoff of KBr and the narrow band MCT detector) was verified to be smaller than the experimental noise. ASW films were too thin to display absorption features due to the weaker overtones and combination bands with $\omega > 3800$ cm^{-1} . The model input parameters are the platinum substrate optical constants,³⁵ the sample optical index of refraction (i.e., n_∞)²⁶ and absolute thickness (i.e., h), the angle of incidence of the infrared beam [$\theta_{\text{IR}} = (82 \pm 1)^\circ$] and a frequency-independent scalar offset to compensate for thermal and electronic detector drift. As discussed in details below, the only adjustable parameter in our model is the absolute sample thickness.

III. Results

RAIRS spectra were recorded for ASW films having a (nominal) coverage of 100 ML (dense ASW equivalent) on Pt(111) at 20 K for θ_{Beam} ranging from normal incidence (0°) to grazing incidence (85°) in 5° increments. These conditions are known to yield dense ASW films for $\theta_{\text{Beam}} < 40^\circ$ and ASW films of increasing porosity for $\theta_{\text{Beam}} > 40^\circ$.^{20–27} Figure 2 displays representative RAIRS spectra for dense (0 and 40°), moderately porous (55°), and highly porous ($75, 80$, and 85°) films over the 800–6500 cm^{-1} available spectral range of the FTIR spectrometer. All spectra display absorption features centered near 900 cm^{-1} (intermolecular librations band), 1600 cm^{-1} (intramolecular HOH bending band), 2200 cm^{-1} (bending/libration combination band), and 3400 cm^{-1} (intramolecular OH stretching band) assigned to coupled vibrational modes of water molecules in the disordered H-bonding network of ASW.^{36,37}

These positive absorbance bands are superimposed on a smoothly decreasing negative absorbance baseline with increasing wavenumbers which arises from destructive interferences (between the multiple reflections at the film–vacuum and film–substrate interfaces) within the ASW film.^{28,29} The greater negative absorbance with increasing wavenumbers arises from two effects: the greater relative optical thickness of the ASW film at shorter wavelengths (yielding larger phase shifts and increasingly destructive interferences) as well as the lower reflectivity of bare platinum for wavenumbers greater than 3500 cm^{-1} . In the inset to Figure 2, we show a magnified view of the dangling OH bonds intramolecular stretching vibrations spectral features peaking at 3695 cm^{-1} (single donor–double acceptor or DAA bonding configurations) and 3720 cm^{-1} (single donor–single acceptor or DA bonding configurations).^{38–40} These spectral features are assigned to under-coordinated water molecules that have one of their intramolecular OH bonds protruding in vacuum (i.e., dangling or free OH) either from the film surface, or from within the films’ porous microstructure.^{38–40}

Surprisingly, only subtle changes in the RAIRS vibrational spectra are observed despite the dramatic decrease in density between films dosed at near normal incidence [$\rho_{\text{ASW}}(\theta_{\text{Beam}} = 0–40^\circ) > 0.90$ g/cm^3] and highly porous samples dosed at glancing angle [$\rho_{\text{ASW}}(\theta_{\text{Beam}} > 70^\circ) < 0.60$ g/cm^3].²⁶ First, the smooth baseline negative slope increases slightly with increasing θ_{Beam} . Second, the amplitude of all absorption features, including that of dangling OH bonds (Figure 2, inset), increases continuously with increasing θ_{Beam} . Finally, there is a slight red-shift in the large absorption feature centered near 3400 cm^{-1} . This red-shift arises from a pronounced increase in absorbance on the lower wavenumbers edge of this broadband which is assigned to coupled H-bonded intramolecular OH stretching vibrations of H_2O molecules within the bulk of ASW.^{36,37}

One could naively interpret the increasing intensity of the dangling bonds spectral features as arising from the greater abundance of molecules with DAA and DA bonding topologies according to the films increasing porosity and surface area at larger θ_{Beam} .^{23,24,27} As a greater total number of water molecules lie at the film–vacuum interface in a porous ASW film comparatively to a dense ASW film, one expects a greater intensity for the dangling OH stretching vibrations spectral features with increasing θ_{Beam} .

In these single donor (i.e., DAA and DA) bonding topologies, under-coordinated surface-bound molecules are expected to have their other intramolecular OH bond engaged in a stronger H-bond with a neighboring H_2O molecule. Such single-donor bonding topologies are known to yield more red-shifted H-bonded OH stretching frequencies along with larger corresponding oscillator strengths than those of fully coordinated (i.e., double donor–double acceptor or DDAA) H_2O molecules in the bulk of ASW.^{41,42} This correlation in the spectral shifts and related intensities of the dangling and H-bonded intramolecular OH stretching vibrations spectral features and greater relative abundance of surface-bound H_2O molecules (DAA and DA) compared to fully coordinated molecules (DDAA) in the bulk of ASW could thus explain the evolution of the RAIRS spectra in the OH stretching range with increasing θ_{Beam} (i.e., increasing porosity and surface area).^{23,24,26}

However, the interpretation of such small changes in the infrared spectra of porous ASW is not straightforward as RAIRS spectra are strongly distorted by trivial optical effects. Specifically, they display a complex interplay between refraction and interference effects (between the multiple reflections at the film–vacuum and film–substrate interfaces) as well as absorption

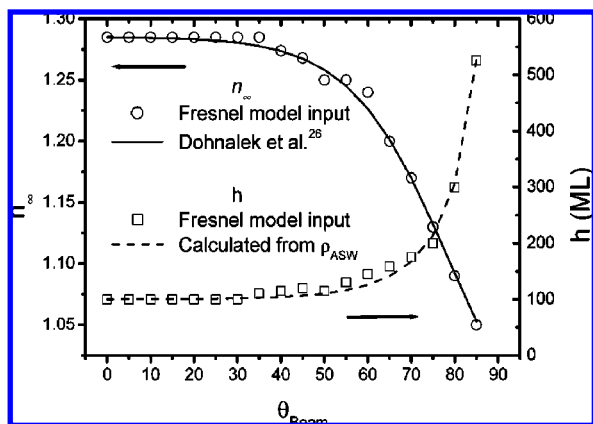


Figure 3. Fresnel model input parameters. Optical indices of refraction, n_{∞} , for molecular beam grown ASW films as a function of θ_{Beam} were taken from ref 26 and fitted to an analytical expression (continuous line, left ordinate). Values used in the model are indicated by open circles. Porous ASW film densities (obtained from their n_{∞} using Lorentz–Lorenz relation) were then used to calculate absolute film thicknesses, h , as a function of θ_{Beam} (dashed line, right ordinate). However, absolute film thicknesses were rather obtained spectroscopically using infrared interferometry (see text) yielding the empirical values shown as open squares (1 ML = 3.67 Å) which show very good agreement with those calculated using the film densities.

within the film.^{30–32} For porous ASW films with complex morphologies, the details of the nanoscale textures are not probed at IR wavelengths ($\lambda > 3 \mu\text{m}$). Thus, at the macroscopic level, evolution in their morphology with increasing θ_{Beam} is only reflected in modulations of their bulk properties namely, as a dramatic decrease in their density and optical indices of refraction, n_{∞} .²⁶ Access to the molecular-level distortions in the H-bonded network of the porous nanostructures of ASW is nevertheless encoded in their RAIRS spectra. However, in order to properly interpret these subtle spectroscopic changes, one needs to untangle the chemically relevant absorption of radiation, through vibrational excitations within the film, from the trivial optical effects inherent to RAIRS. As we will demonstrate below, severe distortions by optical effects in RAIRS spectra complicate their analysis in terms of vibrational spectroscopy to an extent that invalidates the simple qualitative interpretation given above.

We used a simple classical optics model to describe the interaction of the IR beam with nanoscopic ASW films condensed on an optically thick platinum substrate in vacuum. While all ASW films have a constant 100 ML (dense ASW equivalent) coverage (i.e., a surface number density of $\sim 1.25 \times 10^{17} \text{ H}_2\text{O molecules/cm}^2$),⁴³ porous films deposited at large θ_{Beam} have greater absolute physical thicknesses, h , and lower optical indices of refraction, n_{∞} , owing to their lower density, $\rho_{\text{ASW}}(\theta_{\text{Beam}})$.²⁶ As both h and n_{∞} depend on the macroscopic ASW density,²⁶ their values are coupled through the Lorentz–Lorenz (LL) relation and must thus be self-consistently determined. The n_{∞} for molecular beam deposited nanoporous ASW on Pt(111) at 20 K as a function of θ_{Beam} has been measured previously using optical interferometry (i.e., at $\lambda = 6328 \text{ Å}$).²⁶ An analytical expression was obtained by fitting the experimental values and is reported as a continuous line in Figure 3. This expression was used to interpolate n_{∞} as a function of θ_{Beam} , and the values used in our simulations are reported as open circles in Figure 3. Using the LL relation, ρ_{ASW} was determined from their n_{∞} as a function of θ_{Beam} .²⁶ We could therefore evaluate the porous ASW films absolute physical thickness as a function of θ_{Beam} : $h = 100 \text{ ML} \cdot [\rho_{\text{ASW}}(\theta_{\text{Beam}} = 0^\circ) /$

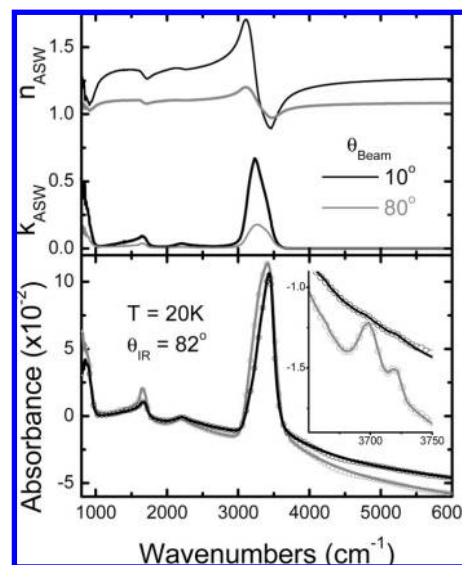


Figure 4. Bottom panel: typical Fresnel model results (continuous line) show excellent agreement with experimental data (open circles, only 1 in 20 data points are shown for clarity) across the whole mid-IR range ($\omega = 800\text{--}6000 \text{ cm}^{-1}$) for both dense ($\theta_{\text{Beam}} = 10^\circ$, black) and highly porous ($\theta_{\text{Beam}} = 80^\circ$, gray) ASW films. The inset shows details of the dangling OH stretching vibrations spectral features. Top panel: frequency-dependent real [i.e., $n_{\text{ASW}}(\omega)$] and imaginary [i.e., $k_{\text{ASW}}(\omega)$] parts of the complex indices of refraction, $\tilde{n}_{\text{ASW}}(\omega)$ for dense ($\theta_{\text{Beam}} = 10^\circ$, black) and highly porous ($\theta_{\text{Beam}} = 80^\circ$, gray) ASW films.

$\rho_{\text{ASW}}(\theta_{\text{Beam}})]$ where the thickness of 1 ML ASW is defined as 3.67 Å. These values are reported as a dashed line in Figure 3.

In our model, however, we treated h as an adjustable parameter. This introduced some flexibility to allow for small fluctuations in the actual molecular beam flux and the resulting film thickness at the various θ_{Beam} . The absolute ASW film thickness was determined using IR interferometry. Specifically, as absorption of IR radiation by thin ASW films is negligible above 4000 cm^{-1} , we adjusted h in the model in order to fit the experimental absorbance in this transparent portion of the RAIRS spectra. The optimal h for films deposited at θ_{Beam} as obtained through IR interferometry are reported as open squares in Figure 3. These empirical values are in very good agreement with the expected film thicknesses calculated using ρ_{ASW} (dashed line).

Using the values of n_{∞} and h reported in Figure 3, and $\theta_{\text{IR}} = 82^\circ$, we modeled the RAIRS spectra of nanoporous ASW films and obtained their frequency-dependent optical constants [$\tilde{n}_{\text{ASW}}(\omega) = n_{\text{ASW}}(\omega) + ik_{\text{ASW}}(\omega)$] at the various θ_{Beam} . Representative results from our simulations for dense ($\theta_{\text{Beam}} = 10^\circ$, black) and highly porous ($\theta_{\text{Beam}} = 80^\circ$, gray) ASW films are reported in Figure 4. In the bottom panel, we compare experimental data (open symbols, 1 in 20 data points are shown for clarity) with simulation results (continuous lines) over the $800\text{--}6000 \text{ cm}^{-1}$ range. The inset shows a magnified view of the dangling OH stretching vibrations spectral region. The frequency-dependent real [i.e., $n_{\text{ASW}}(\omega)$] and imaginary [i.e., $k_{\text{ASW}}(\omega)$] parts of their complex indices of refraction are compared in the upper panel of Figure 4.

Despite the great similarities in the RAIRS spectra of dense and highly porous ASW films (Figure 4, bottom panel), there are several qualitative differences in their optical properties. At first glance, the most striking difference is the much smaller magnitude of the $k_{\text{ASW}}(\omega)$ displayed by the porous film compared to the dense film (Figure 4, upper panel). This can be explained by the much smaller density (i.e., $\rho_{\text{ASW}} \sim 0.31$

versus 0.94 g/cm^3),²⁶ and resulting greater physical thickness ($h = 300 \text{ ML}$ versus 100 ML), of the porous film compared to those of the dense ASW film. Clearly thus, in order for porous ASW films to yield a comparable absorbance to that of dense ASW films having the same (nominal) coverage (Figure 4, bottom panel), thicker porous films must display smaller absorption coefficients [i.e., $k_{\text{ASW}}(\omega)$] than those displayed by the thinner dense films. The smaller $n_{\text{ASW}}(\omega)$ values displayed by porous ASW (Figure 4, upper panel) are simply due to its smaller density and optical index of refraction (see Figure 3).

Another important effect is the qualitatively different peak shapes and positions in the RAIRS spectra for dense and porous ASW (Figure 4, bottom panel) compared to the respective spectral features in their $k_{\text{ASW}}(\omega)$ (Figure 4, upper panel). For example, the amplitude of $k_{\text{ASW}}(\omega)$ for the H-bonded intramolecular OH stretching vibrational band decreases and its peak position shifts to larger wavenumbers, from $k_{\text{max}} = 0.67$ and $\omega = 3233 \text{ cm}^{-1}$ for dense ASW (black), to $k_{\text{max}} = 0.18$ and $\omega = 3267 \text{ cm}^{-1}$ for highly porous ASW (gray). This behavior is exactly opposite to that observed in their absorbance spectra where porous ASW (gray) showed a more intense and red-shifted (i.e., maximum absorbance of 0.114 at $\omega = 3413 \text{ cm}^{-1}$) H-bonded intramolecular OH stretching feature compared to that of dense ASW (black) (i.e., maximum absorbance of 0.106 at $\omega = 3434 \text{ cm}^{-1}$).

The optical effects responsible for this notable distortion of the absorption features in RAIRS are well-known and arise from refraction and anomalous dispersion [i.e., decreasing $n(\omega)$ with increasing wavenumbers] near strong peaks in $k(\omega)$. Specifically, the relative phases of the electronic and nuclear polarizations within the absorbing media change sign across an absorption feature giving rise to the characteristic “first derivative” shape of $n(\omega)$ in the vicinity of a vibrational resonance.⁴⁴ In strongly absorbing ASW, this causes $n_{\text{ASW}}(\omega)$ to become smaller than 1.0 on the blue edge of the coupled H-bonded intramolecular OH stretching vibrations absorption band (i.e., in the $3350\text{--}3550 \text{ cm}^{-1}$ range of Figure 4, top panel). This results in a dramatic increase in the optical path (i.e., negative refraction) in this region of the RAIRS spectra for glancing incidence radiation [i.e., $\theta_{\text{IR}} = 82^\circ$]. Consequently, absorbance features in the RAIRS spectra of nanoscopic ASW films peak at higher wavenumbers than the corresponding peaks in their $k_{\text{ASW}}(\omega)$, an effect that is most pronounced in the intense coupled H-bonded intramolecular OH stretching vibrations spectral range. Furthermore, this effect is much stronger in dense ASW films which display a more intense peak in their $k_{\text{ASW}}(\omega)$, therefore causing a more pronounced anomalous dispersion for $n_{\text{ASW}}(\omega)$ in the vicinity of their intense H-bonded OH stretching absorption feature compared to porous ASW films (Figure 4, top panel). Refraction is thus very strongly coupled to the absorption of infrared radiation within the films and therefore explains the complex relationship between the frequency-dependent optical constants and the RAIRS spectra for ASW films having different densities. Unfortunately, these effects are present even at the smallest film thicknesses and surprisingly, interference effects are noticeable even for increments in film thickness as small as 1 ML for very thin ASW films on platinum. However, complications due to interference effects can be largely circumvented by using substrates which are better reflectors of IR radiation than platinum: gold,³¹ aluminum,³¹ or copper.³² These observations demonstrate the necessity of untangling trivial optical effects from RAIRS spectra for a proper interpretation of their qualitative features.

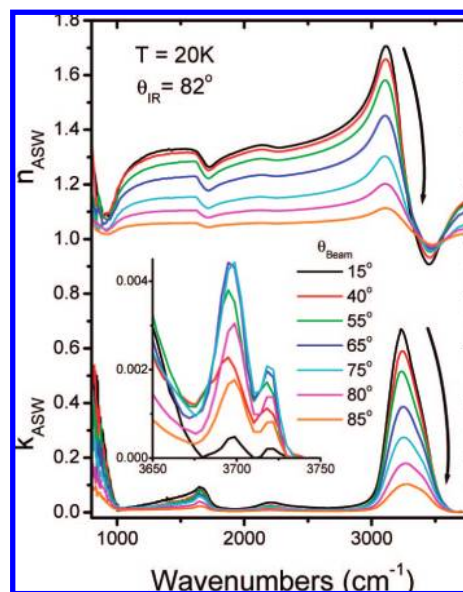


Figure 5. Representative optical constants for molecular beam grown nanoporous ASW films deposited at $\theta_{\text{Beam}} = 15, 40, 55, 65, 75, 80$, and 85° at $T = 20 \text{ K}$ on Pt(111). The inset shows details of $k_{\text{ASW}}(\omega)$ in the dangling OH bonds intramolecular stretching vibrations spectral range. The amplitude of both dangling OH stretching bands is observed to increase up to $65\text{--}75^\circ$ and to decrease with further increases in θ_{Beam} whereas all other absorption bands show a continuously decreasing amplitude with increasing θ_{Beam} .

Finally, Figure 5 displays the optical constants for nanoporous ASW, deposited at selected representative values of θ_{Beam} , obtained from a detailed analysis of their RAIRS spectra (i.e., Figure 4) using our Fresnel model. Optical constants throughout the $1000\text{--}4000 \text{ cm}^{-1}$ range for all deposition incidence angles are available as Supporting Information. In the bottom traces, one observes a monotonic decrease in the amplitude of $k_{\text{ASW}}(\omega)$ with increasing θ_{Beam} , an effect that appears to correlate with the larger h displayed by ASW films with greater porosity (i.e., Figure 3) as discussed previously. On the contrary, the inset to Figure 5 shows that the amplitude of the dangling OH stretching vibrational features in $k_{\text{ASW}}(\omega)$ grows up to $\theta_{\text{Beam}} = 65\text{--}75^\circ$, and then decreases for greater incidence angles. As is seen in the top traces, $n_{\text{ASW}}(\omega)$ decreases continuously across most of the spectral range with increasing θ_{Beam} . This effect is mainly due to the decreasing n_∞ (and density) with increasing θ_{Beam} (i.e., Figure 3).²⁶ The opposite behavior is observed in the vicinities of the “dip” spanning the $3350\text{--}3550 \text{ cm}^{-1}$ range [where $n_{\text{ASW}}(\omega) < 1.0$]: $n_{\text{ASW}}(\omega)$ is seen to increase continuously with θ_{Beam} , following the anomalous dispersion arguments and their relation to the magnitude of the spectral features in $k_{\text{ASW}}(\omega)$ through the KK relation, as discussed above.⁴⁴ In the following discussion, we interpret the complex behavior observed in the spectroscopic features and the optical constants of nanoporous ASW films based on the evolution of their morphological and nanostructural properties with increasing θ_{Beam} .

IV. Discussion

A. Correlation of Optical Properties for Nanoporous ASW Films with Their Morphology. The very strong coupling between trivial optical effects and absorption in RAIRS spectra^{30–32} complicates greatly their interpretation in terms of vibrational spectroscopy for nanoporous ASW films (Figure 2). Using a simple classical optics model to describe RAIRS spectroscopy for molecular beam deposited thin nanoporous

ASW films (Figure 3),^{28,29} we were able to untangle distortions due to refraction and interference effects from chemically relevant absorption in the experimental absorbance spectra (Figure 4). We could thus obtain the frequency-dependent optical parameters (Figure 5) for nanoporous ASW films of known morphologies (i.e., of particular density and surface area).^{23,24,26} The amplitude of the spectral features in $k_{\text{ASW}}(\omega)$ which are associated with coupled H-bonded intramolecular OH stretching vibrations near 3250 cm^{-1} with HOH bending vibrations near 1600 cm^{-1} and with the combination modes near 2200 cm^{-1} all display a continuous decrease with increasing θ_{Beam} . The signal-to-noise ratio is considerably worse for the intermolecular H-bond bending librations band near 900 cm^{-1} ; however, it appears to follow a similar trend. One notes that the decreasing intensity and blue shifting of the spectral feature corresponding to H-bonded intramolecular OH stretching vibrations in $k_{\text{ASW}}(\omega)$ with increasing θ_{Beam} is exactly opposite to what was observed for the corresponding spectral features in the raw RAIRS spectra (Figure 2). Similarly, while the amplitude of the dangling OH stretching vibrations absorbance features increased continuously with θ_{Beam} in the RAIRS spectra (inset to Figure 2), the amplitude of the corresponding spectral features in $k_{\text{ASW}}(\omega)$ increases up to $\theta_{\text{Beam}} = 65\text{--}75^\circ$ and decreases for more grazing incidences (inset in Figure 5). This indicates that the spectral distortions from optical effects inherent to RAIRS can profoundly and qualitatively alter spectroscopic behavior which may yield incorrect interpretations.

The behavior of the optical constants, physical and spectroscopic properties of nanoporous ASW films can be correlated with the evolution in their morphology as a function of increasing θ_{Beam} .^{20–27} While the filamentous texture of nanoporous films grown by molecular beam deposition in the ballistic regime^{21,22} have been characterized extensively (using a variety of complementary techniques ranging from electron microscopy to adsorption isotherms),^{45–54} several of these techniques are not amenable to the characterization of the very fragile nanoporous ASW films. Vibrational spectroscopy is thus the technique of choice being a very sensitive and nondestructive probe. Our quantitative analysis of RAIRS spectra for nanoporous ASW films may therefore provide detailed molecular-level insight into the structure of their H-bonded network.

For example, as the main absorption band centered near 3250 cm^{-1} in $k_{\text{ASW}}(\omega)$ (i.e., Figure 5) arises mostly from coupled H-bonded intramolecular OH stretching vibrations from water molecules in the bulk of ASW, its amplitude should scale with the films' density.²⁶ Accordingly, we integrated the $k_{\text{ASW}}(\omega)$ for the H-bonded intramolecular OH stretching vibrations of ASW across the $2800\text{--}3675\text{ cm}^{-1}$ range for every sample and report the results in Figure 6a (H-bonded OH, full diamonds, left ordinate), along with the film density [ρ_{ASW} , open triangles, right ordinate],²⁶ both as a function of θ_{Beam} . A very strong correlation is observed between the integrated k_{Bonded} and ρ_{ASW} . Although not shown here, the integrated $k_{\text{ASW}}(\omega)$ for the coupled intermolecular librations ($\omega \sim 900\text{ cm}^{-1}$) for the intramolecular HOH bending vibrations ($\omega \sim 1600\text{ cm}^{-1}$) as well as for the combination modes ($\omega \sim 2200\text{ cm}^{-1}$) spectral features also show similarly strong correlations with ρ_{ASW} despite their somewhat poorer signal-to-noise ratio.

This proportionality between the integrated k_{Bonded} for nanoporous ASW films and their macroscopic density indicates that their nanoscale textures may consist of relatively dense ASW domains separated by voids, their relative proportions varying with θ_{Beam} . Such a morphology would be expected if the ballistic deposition conditions used here to grow nanoporous ASW films

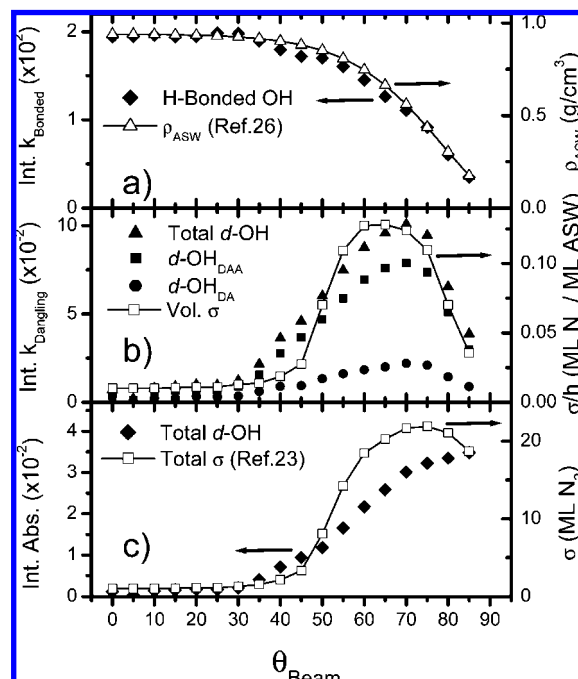


Figure 6. (a) Top panel: Integrated $k_{\text{ASW}}(\omega)$ for the H-bonded OH stretching vibrations spectral feature (\blacklozenge , k_{Bonded} , left ordinate) are compared with nanoporous ASW films densities (\triangle , ρ_{ASW} , right ordinate)²⁶ as a function of the H_2O molecular beam incidence angle, θ_{Beam} . (b) Middle panel: Integrated $k_{\text{ASW}}(\omega)$ for the dangling OH stretching vibrations spectral features (\blacktriangle , total $d\text{-OH}$; \blacksquare , $d\text{-OH}_{\text{DAA}}$; \bullet , $d\text{-OH}_{\text{DA}}$, left ordinate) are compared with nanoporous ASW film volumetric effective surface area (\square , vol. σ , right ordinate) as a function of the H_2O molecular beam incidence angle, θ_{Beam} . (c) Bottom panel: Total (calculated) integrated absorbance for the dangling OH stretching vibrations spectral features (\blacklozenge , total $d\text{-OH}$, left ordinate) are compared with nanoporous ASW films total effective surface area (\square , total σ , right ordinate)²³ as a function of the H_2O molecular beam incidence angle, θ_{Beam} .

yielded nanoscale textures analogous to those displayed by the well-characterized nanoporous metals, semiconductors, or oxides thin films grown by glancing angle deposition (GLAD).^{45–54} By analogy therefore, the behavior of the optical properties of nanoporous ASW films with their density is consistent with their nanoscale textures consisting of dense ASW columns of increasing height (i.e., Figure 3), that become separated by increasing distances with increasing θ_{Beam} yielding greater porosities and a smaller densities.^{21,22}

Following similar arguments, as the dangling bonds intramolecular OH stretching spectral features in $k_{\text{ASW}}(\omega)$ are the vibrational spectroscopic signatures of surface-bound H_2O molecules (adopting either DAA and DA bonding topologies),^{38–40} their amplitude should correlate with the films volumetric surface area.^{23,24} Therefore, Figure 6b reports the integrated $k_{\text{ASW}}(\omega)$ for the dangling OH stretching vibrations spectral features, k_{Dangling} , for molecules in the DAA ($d\text{-OH}_{\text{DAA}}$ peaking at $\omega \sim 3695\text{ cm}^{-1}$, full squares - left ordinate) and in the DA ($d\text{-OH}_{\text{DA}}$ peaking at $\omega \sim 3720\text{ cm}^{-1}$, full circles - left ordinate) bonding topologies, as well as their sum (total $d\text{-OH}$, full triangles - left ordinate), as a function of θ_{Beam} .

A quantitative evaluation of the effective surface area of molecular beam deposited nanoporous ASW as a function of θ_{Beam} was recently reported using nitrogen uptake experiments.^{23,24} The effective surface area, σ , of a (nominally) 100 ML (dense ASW equivalent) coverage nanoporous ASW film (expressed in terms of the saturated nitrogen coverage, ML N_2 , required to occupy all its surface adsorption sites), was evaluated as a

function of θ_{Beam} .^{23,24} Since the films' effective surface area scales linearly with sample thickness, k_{Dangling} should rather be compared to a thickness-invariant physical property: the volumetric effective surface area. To compare with the integrated k_{Dangling} , σ was therefore divided by the nanoporous ASW films absolute physical thickness, h (i.e., Figure 3), yielding a volumetric effective surface area expressed in N₂ coverage per unit of nanoporous ASW film physical thickness (i.e., in ML N₂ per ML nanoporous ASW) and is reported as a function of θ_{Beam} in Figure 6b (σ/h , open squares - right ordinate). A fair correlation is observed between the integrated $k_{\text{ASW}}(\omega)$ for dangling OH spectral features and the nanoporous ASW films volumetric effective surface area.

Surprisingly, while the porosity (i.e., Figure 3 and 6a)²⁶ and the amplitude of the dangling OH bonds absorbance features of nanoporous ASW films (i.e., Figure 2)²⁷ increase continuously with increasing θ_{Beam} , both their volumetric effective surface area (as measured by nitrogen physisorption)^{23,24} and their integrated k_{Dangling} present a maximum at around $\theta_{\text{Beam}} = 65\text{--}70^\circ$ (i.e., Figure 6b). The simple morphological model presented above (based on ballistic deposition simulation and on the known nanoscale textures of thin metallic, semiconducting or oxide films grown by GLAD)^{45–54} and used to interpret the behavior of the integrated k_{Bonded} with θ_{Beam} may also provide a qualitative interpretation for such a peculiar evolution of the integrated k_{Dangling} as a function of θ_{Beam} . The effective surface area displayed by a (nominally) 100 ML (dense ASW equivalent) coverage nanoporous ASW film starts out at 1 ML N₂ for dense films ($\theta_{\text{Beam}} = 0\text{--}30^\circ$) that adsorb nitrogen only on their outermost surface. As θ_{Beam} increases from 30 to 60° , ballistic deposition simulations of molecular beam grown ASW films showed^{21,22} the formation of an extended interconnected nanoporous network between dense ASW columns within the growing porous films. This porous network gives rise to the large increase in the films surface area^{23,24} and the strong decrease in their density²⁶ for increasing θ_{Beam} up to $\sim 60^\circ$. For still larger θ_{Beam} , ballistic deposition simulations^{21,22} showed that individual columns should grow to greater lengths and thus yield thicker films (i.e., Figure 3). At these grazing incidences, the resulting increase in their shadowing effects should also yield a greater separation between individual dense ASW columns and an increased pore volume yielding a decreasing macroscopic density for nanoporous ASW (Figure 6a) deposited at increasing θ_{Beam} .²⁶ However, assuming the cross sectional area of individual columns remains constant as a function of θ_{Beam} , this would yield a constant total surface area for ASW films deposited at $\theta_{\text{Beam}} > 60^\circ$.^{23,24,27} Therefore, the decreasing surface number density of dense ASW columns resulting from the increasing pore volume would result in a decreasing volumetric surface area with increasing θ_{Beam} (i.e., Figure 6b). This morphological model may thus explain why the integrated k_{Dangling} and the ASW films volumetric surface area reach a maximum around $\theta_{\text{Beam}} = 65\text{--}70^\circ$ and then decline at the most grazing angles (i.e., Figure 6b) while the films density decreases continuously (i.e., Figure 6a) with increasing θ_{Beam} .

Finally, Figure 6c presents the total integrated absorbance [$\alpha(\omega) \cdot h = 4\pi\omega k(\omega) \cdot h$] from dangling OH bonds, calculated using optical constants for nanoporous ASW films (Figure 5) and integrated over their dangling bonds OH stretching spectral features, as a function of θ_{Beam} (total *d*-OH, full diamonds - left ordinate). As this property describes the total absorbance from all the dangling OH bonds within the nanoporous ASW film of absolute physical thickness h , this property should be compared with their total effective surface area, σ .^{23,24} This latter

is presented in Figure 6c [in units of the saturated nitrogen coverage (i.e., ML N₂) for a (nominally) 100 ML (dense ASW equivalent) coverage nanoporous ASW film] as a function of θ_{Beam} (σ , open squares - right ordinate).^{23,24} A fair correlation is observed between the total integrated absorbance from all the nanoporous ASW films dangling bonds OH stretching spectral features and their *total* effective surface area.^{23,24}

In nitrogen (and other weakly physisorbed species) adsorption,^{20–27} the contribution from capillary condensation (which may allow for multilayer adsorption in the intermediate sized pores formed at $\theta_{\text{Beam}} = 45\text{--}70^\circ$ incidence through the Kelvin effect) is difficult to distinguish from physisorption onto the extended interconnected nanoporous network internal surface area within the ASW films. One may therefore argue that a spectroscopic determination of the surface area for nanoporous ASW films provides a more reliable evaluation of this property. Therefore, the decreasing apparent volumetric (Figure 6b, open squares) and total (Figure 6c, open squares) effective surface area for $\theta_{\text{Beam}} > 65\text{--}75^\circ$ observed by nitrogen adsorption may stem from a decreasing contribution from capillary condensation within the very large pores created by molecular beam deposition at these most grazing incidence angles.^{20–27} Finally, one concludes that different but complementary properties of nanoporous ASW films are probed by N₂ physisorption and IR spectroscopic experiments which explains the somewhat poorer correlation between surface area measurements performed by these two methods (i.e., Figure 6b and 6c) than that observed between the integrated k_{Bonded} and the density of ASW (i.e., Figure 6a).

B. Comparison with previously published optical parameters for ASW. The optical constants reported here for ASW should be compared to the most widely used spectroscopic data by the astrophysical community, namely those of Hudgins et al.¹⁷ and those of Léger et al.¹⁵ These latter authors used backfilling of their vacuum chamber to grow ASW films (0.5–1 μm thick at a maximum rate of 20 $\mu\text{m/hr}$) by vapor deposition on a high purity silicon substrate maintained at $T = 77\text{ K}$. Hudgins et al.¹⁷ used a tube doser to grow their sample (0.41 μm thick at a rate of 2.6 $\mu\text{m/hr}$) on a CsI substrate at $T = 10\text{ K}$ (and then heated them to $T = 40, 80, 100, 120$, and finally 140 K). Both these preparation methods may have yielded some adsorption on both the front and rear surfaces of the transparent substrate. The absolute sample thickness was determined by optical interferometry but neither author reported the density of their samples. Transmission absorption spectra were acquired at normal incidence ($\theta_{\text{IR}} = 0^\circ$) and at the deposition temperature (as well as at the subsequent annealing temperatures by Hudgins et al.).¹⁷ Léger et al.¹⁵ used $n_\infty = 1.31$, while Hudgins et al.¹⁷ used $n_\infty = 1.32$, in KK transforms in order to derive the optical constants of their ASW films.

The optical parameters reported here for dense ASW (i.e., $\theta_{\text{Beam}} = 0\text{--}30^\circ$) agree quite well with those reported by Léger et al.:¹⁵ our values for $k_{\text{ASW}}(\omega)$ are within -3 to $+7\%$ of theirs in the H-bonded OH stretching range (i.e., 3060–3410 cm^{-1}), within -15 to 0% for the HOH bending range (i.e., 1500–1700 cm^{-1}), and within 0 to $+15\%$ for the combination band range (i.e., 2100–2570 cm^{-1}). Unfortunately, our data are too noisy below 1000 cm^{-1} to allow a meaningful comparison in the intermolecular librations range. Given the deposition temperature and flux used by Leger et al. to grow their samples (i.e., $T = 77\text{ K}$ and $\sim 15\text{ ML/sec}$, respectively),¹⁵ a relatively dense ASW film should have formed on their substrate.^{20–27} This may explain the similarities between the optical constants they reported and those obtained here for dense ASW (i.e., at $T =$

20 K for $\theta_{\text{Beam}} = 0\text{--}30^\circ$ and a maximum flux of ~ 0.87 ML/sec) despite the fact that they used a large $n_\infty = 1.31$ in the KK transform (see Figure 3). Furthermore, in experiments to be reported elsewhere, only a very weak temperature dependence was observed between $T = 20$ and 120 K in the RAIRS spectra of dense ASW which further validates the similarities between their optical constants obtained at $T = 77$ K and those reported here for dense ASW at $T = 20$ K. Finally, the $n_{\text{ASW}}(\omega)$ obtained here agree to within -5.5 to $+2\%$ across the whole $1000\text{--}4000$ cm^{-1} range with those reported by Leger et al. (including their $\sim 2\%$ systematic overestimation in n_∞).¹⁵

A comparison with the optical constants reported by Hudgins et al.¹⁷ is more difficult because of important differences in the preparation method (i.e., substrate temperature of 10 K and flux near 2 ML/sec), resulting in uncertainties over the sample morphology as well as the high $n_\infty = 1.32$ used in the KK transform. At this much lower temperature, their films may have been initially porous. Indeed, the optical constants they reported¹⁷ for the “as grown” film at $T = 10$ K matches most closely those obtained here at $\theta_{\text{Beam}} = 60^\circ$ and $T = 20$ K (i.e., $\sim 25\%$ porous or $\rho_{\text{ASW}} \sim 0.75$ g/cm^3). The initial porosity of their sample is also supported by the very large dangling OH stretching vibrations spectral feature in their $k_{\text{ASW}}(\omega)$ that peaks at $\omega \sim 3665$ cm^{-1} .¹⁷ This very red-shifted dangling OH stretching frequency could be evidence of contaminants being adsorbed on their sample. For example, N_2 -covered ASW films yield a dangling OH peak centered at $\omega \sim 3672$ cm^{-1} .^{23,24} The presence of internal porosity and of surface contamination may thus have affected the evaluation of the optical constants of their “as grown” sample at $T = 10$ K. Upon heating to $T = 40, 80$, and 100 K, such an initially porous films would have densified resulting in a loss of intensity in the dangling OH stretching vibrations spectral feature and concomitantly, an increase in the coupled H-bonded intramolecular OH stretching vibrations spectral feature in $k_{\text{ASW}}(\omega)$.²⁷ This is precisely what is observed in the data of Hudgins et al.¹⁷ suggesting that what they reported as temperature-dependent optical constants are rather strongly affected by morphological relaxation of an initially porous sample upon thermal annealing.²⁷ This could have been easily verified by cooling the sample to lower temperature after annealing in order to verify whether these spectroscopic changes were reversible. Finally, the optical constants they reported for ASW at $T = 100$ and 120 K are still not consistent with those obtained here for fully dense ASW ($\theta_{\text{Beam}} = 0\text{--}30^\circ$) relying again on our observations of a very weak temperature dependence of the absorbance spectra of dense ASW. While $k_{\text{ASW}}(\omega)$ at these higher temperatures do not display any spectral signature from dangling OH bonds, thereby suggesting they may be dense, they resemble most those obtained here for $\theta_{\text{Beam}} = 40^\circ$ at $T = 20$ K (i.e., 4% porous or $\rho_{\text{ASW}} \sim 0.9$ g/cm^3).²⁶ We believe uncertainties in sample morphologies and possible contamination issues render any further comparisons impossible.

C. Spectroscopic Characterization of Nanoporous ASW Films H-Bonded Network: RAIRS Is Not a Pure Vibrational Spectroscopy. Using the optical constants obtained with our Fresnel model (i.e., Figure 5), we calculated the Beer–Lambert absorptivity, $\alpha(\omega) = 4\pi\omega k(\omega)$, and the absorbance spectra, $\alpha(\omega) \cdot h = -\log [I(\omega)/I_0(\omega)]$, for nanoporous films having a (nominal) coverage of 100 ML (dense ASW equivalent) and report their intramolecular OH stretching spectral region in Figure 7a. These (theoretical) absorbance spectra can be interpreted in terms of the vibrational spectra for free-standing nanoporous ASW films that would be observed in normal incidence transmission absorption infrared spectroscopy [i.e.,

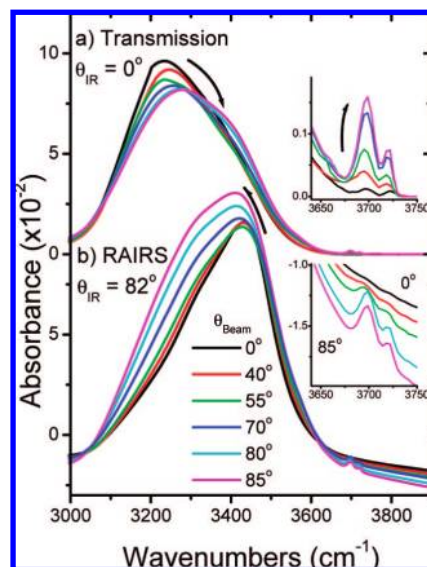


Figure 7. (a) Theoretical normal incidence transmission absorbance spectra modeled using the nanoporous ASW empirical optical constants (i.e., Figure 5). These spectra represent the infrared vibrational spectra expected from free-standing (nominally) 100 ML (dense ASW equivalent) coverage nanoporous ASW films (without the contributions from reflection losses and interference effects). Spectra are constructed from empirical optical constants by multiplying the Beer–Lambert absorptivity, $\alpha(\omega) = 4\pi\omega k(\omega)$ by the absolute film thickness, h : $A(\omega) = \alpha(\omega) \cdot h = -\log[I(\omega)/I_0(\omega)]$. (b) The raw experimental absorbance RAIRS spectra from Figure 2 are reproduced for comparison. Insets show details of the dangling bonds intramolecular OH stretching vibrations spectral range.

$\theta_{\text{IR}} = 0^\circ$] if one could avoid the complexities arising from trivial optical effects (i.e., refraction and reflection losses as well as interferences arising from multiple reflections at the film–vacuum interfaces). The corresponding RAIRS absorbance spectra are reproduced in Figure 7b for comparison.

While the amplitude of the dangling OH bands shows a qualitatively similar continuous increase with increasing θ_{Beam} , as well as identical peak positions, in both transmission (Figure 7a, inset) and RAIRS (Figure 7b, inset) spectra, their amplitude is almost twice as large in the latter. This rather similar behavior for the dangling OH bonds spectral features in both RAIRS and vibrational spectra is to be contrasted with that of the H-bonded OH bonds spectral feature. One observes that the very intense band assigned to coupled H-bonded OH stretching vibrations in the vibrational spectra of nanoporous ASW (Figure 7a) blue shifts only slightly, and that its intensity decreases only slightly, with increasing θ_{Beam} despite the dramatic decrease in ASW density (i.e., relative density falling from 100% down to below 20%; Figure 6a). Interestingly, one notes that this behavior is exactly opposite to what is observed in the RAIRS spectra (Figure 7b): the large H-bonded OH stretching band red shifts, and its intensity increases with increasing θ_{Beam} . One also immediately observes the conspicuous ~ 200 cm^{-1} blue shift of the absorbance maxima in the RAIRS spectra (Figure 7b) compared to those of the corresponding vibrational spectra (Figure 7a). As discussed previously, the optical distortions inherent to RAIRS are most pronounced in the large H-bonded OH stretching spectral range of ASW due to the large anomalous dispersion effects, and related negative refraction. These distortions are so severe that they invalidate the simple qualitative preliminary interpretation proposed earlier based on the evolution of the intramolecular (H-bonded and dangling) OH stretching vibrations spectral features with increasing θ_{Beam} observed

in RAIRS spectra (Figure 2). Therefore, this demonstrates that RAIRS spectra cannot be straightforwardly interpreted as pure vibrational spectra.

The small blue shift and corresponding small intensity decrease of the H-bonded OH stretching band observed in the vibrational spectra of nanoporous ASW films (Figure 7a) as a function of increasing θ_{Beam} indicate that the H-bonded network of highly porous ASW is only slightly weaker and more strained than that of dense ASW. This conclusion follows those drawn by Devlin, Buch and collaborators⁵⁵ to explain the continuous blue shift of the H-bonded OH stretching band observed in the vibrational spectra of ice nanoparticles of decreasing sizes. Such small changes in the vibrational spectra of nanoporous ASW films that display a dramatic decrease in density and increase in surface area with increasing θ_{Beam} therefore support the hypothesis that they are formed by nanoscopic domains (i.e., filaments or columns) of dense ASW separated by voids.^{20–27} On the other hand, the amplitude of the spectral features from dangling OH bonds intramolecular stretching vibrations in the vibrational spectra increases continuously with increasing porosity and saturates at large θ_{Beam} (see also Figure 6c), similar to the behavior reported in the raw absorbance spectra (Figure 2). Our spectroscopic determination of molecular beam deposited nanoporous ASW films total surface area thus also supports the suggestion from ballistic deposition simulations^{21,22} that it increases rapidly for increasing θ_{Beam} from 30 to 60°, but then levels off at more grazing incidence. Spectroscopic observations reported herein are thus consistent with the proposed morphological model suggesting the nanoscale texture of molecular beam deposited porous ASW is analogous to that of other more refractory materials^{45–54} and which consists of columns of increasing length but similar cross sectional area yielding a relatively constant surface area for $\theta_{\text{Beam}} > 70^\circ$, but a continuously decreasing density with increasing θ_{Beam} .

Finally, as the number density of H₂O molecules is constant for all the nanoporous ASW films whose (theoretical) vibrational spectra are reported in Figure 7a, one expects that the gain in oscillator strength from surface-bound H₂O molecules (Figure 6c) should come at the expense of that from H₂O molecules in the bulk of ASW as the films' porosity and surface area increase. The effect of such a conversion of bulk-like molecules to surface-like molecules with increasing surface area in nanoporous ASW films should result in a decrease in the amplitude of the H-bonded intramolecular OH stretching vibrations absorbance spectral feature as a function of θ_{Beam} concomitantly with the increase in the amplitude of the dangling OH intramolecular stretching vibrations spectral features in Figure 7a. Surprisingly, the 10-fold increase in the integrated absorbance from dangling OH bonds (Figure 6c) between dense ASW and the most porous films does not result in a measurable decrease in the integrated absorbance of the coupled H-bonded intramolecular OH stretching band (data not shown). This can be explained by the ca. 100-fold greater (average) oscillator strength of H-bonded OH stretching vibrations relative to those of dangling OH stretching vibrations. Therefore, despite a 20-fold increase in the surface area of nanoporous ASW films as a function of increasing θ_{Beam} (Figure 6c), and the concomitant 10-fold decrease in their density (Figure 6a), the small (<10%) expected decrease in the total integrated absorbance from H-bonded OH stretching vibrations spectral feature is obscured by the cumulative uncertainties in the optical constants and the films thicknesses used in calculating the (theoretical) transmission absorption spectra reported in Figure 7a.

V. Conclusions

The detailed quantitative interpretation presented herein highlights the complex interplay between interference effects, refraction, and absorption in the RAIRS spectra of porous ASW films and the difficulties in their spectroscopic characterization. These trivial optical effects conspire to cause severe distortions in RAIRS spectra which preclude their interpretation in terms of vibrational spectroscopy. In this work, complete spectroscopic characterization of nanoporous ASW films using infrared interferometry and vibrational spectroscopy has been performed concomitantly using RAIRS. A quantitative interpretation of their optical constants was provided using a simple classical optics model based on Fresnel equations and shown to correlate strongly with the films morphological characteristics. Namely, the integrated $k_{\text{ASW}}(\omega)$ for the H-bonded intramolecular OH stretching band near 3250 cm⁻¹, of the intramolecular HOH bending band near 1600 cm⁻¹, of the combination band near 2200 cm⁻¹, and of the intermolecular librations band near 900 cm⁻¹ were all shown to scale with the density of molecular beam deposited nanoporous ASW films. On the other hand, the integrated $k_{\text{ASW}}(\omega)$ for the dangling bonds intramolecular OH stretching vibrations spectral features followed a similar trend to that of their (volumetric and total) effective surface area as measured by nitrogen adsorption. Using these optical constants, (theoretical) vibrational spectra were calculated highlighting the severe optical distortions inherent to RAIRS and providing a detailed microscopic look at the evolution of the H-bonded network of nanoporous ASW films with their increasing porosity and surface area. The optical constants reported here could allow astrophysicists to correlate the spectroscopic properties of amorphous ices with their growth conditions in the ISM and with the resulting physical and morphological parameters of these important molecular solids. Clearly however, as astrophysical ices are unlikely to be constituted of neat ASW, the effect of impurities on their optical constants should be investigated experimentally as reported previously.^{16,17} For simple inert solutes, optical constants of "dirty" ices may be represented relatively well from those of the pure solids using mixing rules.¹⁶ This approach should provide better estimates for those mixed molecular solids involving molecules (i.e., CO, CH₄, and so forth) that either do not react with ASW or which phase separate and form inclusions. These solutes may then display vibrational frequencies and oscillator strengths that are similar to those characterizing the neat solids and thus provide a straightforward contribution to the spectral properties of mixed molecular solids. For solutes that interact strongly with ASW (NH₃, HF, and so on),^{16,28} mixing rules do not provide an appropriate approximation for the optical constants of these complex molecular solids that thus need to be experimentally investigated as a function of all relevant parameters (temperature, composition, and so forth) in order to provide a proper account of their optical properties. As better spectroscopic observations of the ISM become available, these optical constants may contribute to improve our understanding of the complex heterogeneous chemistry processes that take place at the surface of icy bodies in the ISM.

Acknowledgment. This work was supported by the U.S. Department of Energy (DOE), Office of Basic Energy Sciences, Chemical Science Division. The experiments were performed at the W.R. Wiley Environmental Molecular Sciences Laboratory, a national scientific user facility sponsored by DOE's Office of Biological and Environmental Research and located at Pacific Northwest National Laboratory, which is operated for DOE by Battelle. P.A. acknowledges support from the National

Science and Engineering Research Council (NSERC) of Canada and the Canadian Foundation for Innovation.

Supporting Information Available: Real and imaginary parts of the complex index of refraction for ASW deposited at the various incidence angle are reported throughout the 1000–4000 cm^{-1} range at 4 cm^{-1} resolution. Relative uncertainties for the real and imaginary parts are estimated to be ~ 5 and $\sim 2\%$, respectively. This material is available free of charge via the Internet at <http://pubs.acs.org>.

References and Notes

- (1) Allamandola, L. J.; Bernstein, M. P.; Sandford, S. A.; Walker, R. L. *Space Sci. Rev.* **1999**, *90*, 219.
- (2) Palumbo, M. E. *J. Phys.: Conf. Series* **2005**, *6*, 211.
- (3) Jenniskens, P.; Blake, D. F. *Science* **1994**, *265*, 753.
- (4) Klinger, J. *J. Phys. Chem.* **1983**, *87*, 4209.
- (5) Delsemme, A. H. *J. Phys. Chem.* **1983**, *87*, 4214.
- (6) Batista, E. R.; Ayotte, P.; Bilić, A.; Kay, B. D.; Jónsson, H. *Phys. Rev. Lett.* **2005**, *95*, 223201.
- (7) Brown, D. E.; George, S. M.; Huang, C.; Wong, E. K. L.; Rider, K. B.; Smith, R. S.; Kay, B. D. *J. Phys. Chem.* **1996**, *100*, 4988.
- (8) Smith, R. S.; Kay, B. D. *Surf. Sci. Rev.* **1997**, *4*, 781.
- (9) Dijkstra, C.; Dominik, C.; Hoogzaad, S. N.; de Koter, A.; Min, M. *Astron. Astrophys.* **2003**, *401*, 599.
- (10) Dijkstra, C.; Dominik, C.; Bouwman, J.; de Koter, A. *Astron. Astrophys.* **2006**, *449*, 1101.
- (11) Ayotte, P.; Smith, R. S.; Stevenson, K. P.; Dohnálek, Z.; Kimmel, G. A.; Kay, B. D. *J. Geophys. Res.-Planets* **2001**, *106*, 33387.
- (12) Hornekaer, L.; Baurichter, A.; Petrunin, V. V.; Luntz, A. C.; Kay, B. D.; Al-Halabi, A. *J. Chem. Phys.* **2005**, *122*, 124701.
- (13) Azria, R.; Le Coat, Y.; Lachgar, M.; Tronc, M.; Parenteau, L.; Sanche, L. *Surf. Sci.* **1999**, *436*, L671.
- (14) Bar-Nun, A.; Dror, J.; Kochavi, E.; Laufer, D. *Phys. Rev. B* **1987**, *35*, 2427.
- (15) Léger, A.; Gauthier, S.; Défourneau, D.; Rouan, D. *Astron. Astrophys.* **1983**, *117*, 164.
- (16) Mukai, T.; Krätschmer, W. *Earth, Moon, Planets* **1986**, *36*, 145.
- (17) Hudgins, D. M.; Sandford, S. A.; Allamandola, L. J.; Tielens, A. G. G. M. *Astrophys. J., Suppl. Ser.* **1993**, *86*, 713.
- (18) Dartois, E. *Space Sci. Rev.* **2005**, *119*, 293.
- (19) Newman, S. F.; Buratti, B. J.; Brown, R. H.; Jaumann, R.; Bauer, J.; Momary, T. *Icarus* **2008**, *193*, 397.
- (20) Stevenson, K. P.; Kimmel, G. A.; Dohnálek, Z.; Smith, R. S.; Kay, B. D. *Science* **1999**, *283*, 1505.
- (21) Kimmel, G. A.; Stevenson, K. P.; Dohnálek, Z.; Smith, R. S.; Kay, B. D. *J. Chem. Phys.* **2001**, *114*, 5384.
- (22) Kimmel, G. A.; Dohnálek, Z.; Stevenson, K. P.; Smith, R. S.; Kay, B. D. *J. Chem. Phys.* **2001**, *114*, 5295.
- (23) Zubkov, T.; Smith, R. S.; Engstrom, T. R.; Kay, B. D. *J. Chem. Phys.* **2007**, *127*, 184707.
- (24) Zubkov, T.; Smith, R. S.; Engstrom, T. R.; Kay, B. D. *J. Chem. Phys.* **2007**, *124*, 184708.
- (25) Smith, R. S.; Zubkov, T.; Kay, B. D. *J. Chem. Phys.* **2006**, *124*, 114710.
- (26) Dohnálek, Z.; Kimmel, G. A.; Ayotte, P.; Smith, R. S.; Kay, B. D. *J. Chem. Phys.* **2003**, *118*, 364.
- (27) Smith, R. S.; Zubkov, T.; Dohnálek, Z.; Kay, B. D. *J. Phys. Chem. B*, in press.
- (28) Ayotte, P.; Plessis, S.; Marchand, P. *Phys. Chem. Chem. Phys.* **2008**, *10*, 4785.
- (29) Ifimie, R.; Thomas, V.; Plessis, S.; Marchand, P.; Ayotte, P. *J. Am. Chem. Soc.* **2008**, *130*, 5901.
- (30) Toon, O. B.; Tolbert, M. A.; Koehler, B. G.; Middlebrook, A. M.; Jordan, J. *J. Geophys. Res.* **1994**, *99*, 25631.
- (31) Maté, B.; Medialdea, A.; Moreno, M. A.; Escibano, R.; Herrero, V. *J. J. Phys. Chem. B* **2003**, *107*, 11098.
- (32) Mitlin, S.; Leung, K. T. *Can. J. Chem.* **2004**, *82*, 978.
- (33) Schlichting, H.; Menzel, D. *Rev. Sci. Instrum.* **1993**, *64*, 2013.
- (34) Daschbach, J. L.; Peden, B. M.; Smith, R. S.; Kay, B. D. *J. Chem. Phys.* **2004**, *120*, 1516.
- (35) Lynch, W.; Hunter, W. R. *Handbook of optical constants of solids*; Academic press: Orlando, 1985.
- (36) Rowland, B.; Kadagathur, N. S.; Devlin, J. P.; Buch, V.; Feldman, T.; Wojcik, M. *J. J. Chem. Phys.* **1995**, *102*, 8328.
- (37) Devlin, J. P.; Buch, V. *J. Phys. Chem.* **1995**, *99*, 16534.
- (38) Rowland, B.; Devlin, J. P. *J. Chem. Phys.* **1991**, *94*, 812.
- (39) Rowland, B.; Fisher, M.; Devlin, J. P. *J. Chem. Phys.* **1991**, *95*, 1378.
- (40) Buch, V.; Devlin, J. P. *J. Chem. Phys.* **1991**, *94*, 4091.
- (41) Buch, V. *J. Phys. Chem. B* **2005**, *109*, 17771.
- (42) Gruenloh, C. J.; Carney, J. R.; Arrington, C. A.; Zwier, T. S.; Fredericks, S. Y.; Jordan, K. D. *Science* **1997**, *276*, 1678.
- (43) Zimbitas, G.; Haq, S.; Hodgson, A. *J. Chem. Phys.* **2005**, *123*, 174701.
- (44) Feynman, R. P. *The Feynman lectures on physics*; Addison-Wesley: Reading, MA, 1963; Vol. 2.
- (45) Dirks, A. G.; Leamy, H. J. *Thin Solid Films* **1977**, *47*, 219.
- (46) Dohnálek, Z.; Kimmel, G. A.; McCreedy, D. E.; Young, J. S.; Dohnálová, A.; Smith, R. S.; Kay, B. D. *J. Phys. Chem. B* **2002**, *106*, 3526.
- (47) Kim, J.; Dohnálek, Z.; Kay, B. D. *Surf. Sci.* **2005**, *586*, 137.
- (48) Flaherty, D. W.; Dohnálek, Z.; Dohnálová, A.; Arey, B. W.; McCreedy, D. E.; Ponnusamy, N.; Mullins, C. B.; Kay, B. D. *J. Phys. Chem. C* **2007**, *111*, 4765.
- (49) Abelmann, L.; Lodder, C. *Thin Solid Films* **1997**, *305*, 1.
- (50) Robbie, K.; Brett, M. J. *J. Vac. Sci. Technol., A* **1997**, *15*, 1460.
- (51) Robbie, K.; Sit, J. C.; Brett, M. J. *J. Vac. Sci. Technol., B* **1998**, *16*, 1115.
- (52) Messier, R.; Gehrke, T.; Frankel, C.; Venugopal, V. C.; Otaño, W.; Lakhtakia, A. *J. Vac. Sci. Technol., A* **1997**, *15*, 2148.
- (53) Hodgkinson, I.; Wu, Q. H.; Hazel, J. *Appl. Opt.* **1998**, *37*, 2653.
- (54) van Kranenburg, H.; Lodder, C. *Mat. Sci. Eng., R* **1994**, *11*, 295.
- (55) Buch, V.; Bauerecker, S.; Devlin, J. P.; Buck, U.; Kazimirski, J. K. *Int. Rev. Phys. Chem.* **2004**, *23*, 375.

JP806738A